IEEE Access
Multidisciplinary | Rapid Review | Open Access Journal

Received November 1, 2019, accepted November 15, 2019, date of publication November 20, 2019, date of current version December 4, 2019.

Digital Object Identifier 10.1109/ACCESS.2019.2954625

Online Correction Method for Ratio Methods by Using Geomagnetic Sensors Based on Kalman Filter

WEI WANG AND YULIN LIU
National Key Laboratory of Transient Physics, Nanjing University of Science and Technology, Jiangsu 210094, China
Corresponding author: Wei Wang (office2007@njust.edu.cn)

This work was supported by the Science and Technology on Electronic Test & Measurement Laboratory opening fund under Grant 614200104021017.

ABSTRACT By eliminating the data offset caused by a disturbing magnetic field during the flying condition of a spinning projectile, an adaptive unscented Kalman filter is applied to estimate the actual data of a geomagnetic field and the false value introduced by a disturbing magnetic field. For the ratio methods related to geomagnetic attitude measurement, the physical significance of the ratios obtained by all ratio methods is clarified. A new definition for the ratio is presented to ensure online estimation and numerical stability. The variation in the sensor outputs along the lateral directions is suggested to be a harmonic motion with the assumption that the spindle is fixed or in slow motion. The true data employed as a reference for comparison is generated by a dynamics model for spinning objects and by projecting the geomagnetic field to the measurement frame. Signal gathering and data preprocessing are considered. A signal-disturbing ratio is introduced to indicate the proportions of the real geomagnetic signal and the interference signal in the data acquisition process. The algorithm of the adaptive unscented Kalman filter is discussed. Simulations are performed using a 1 kHz sample rate and a duration of 60 seconds. The filtering results supported by a conventional unscented Kalman filter and adaptive unscented Kalman filters are compared with actual data for the conditions of different signal-disturbing ratios and 10 shifts of the disturbing magnetic field. The results of the simulation indicate that the proposed adaptive unscented Kalman filter with the introduced state equation achieves better performance than other filters mentioned in the paper. The filter has the ability to provide clean data from the noisy data flow measured from a spinning projectile for the ratio methods based on the geomagnetic measurements.

INDEX TERMS Geomagnetic measurement, attitude estimation, Kalman filter, data correction, ratio methods.

I. INTRODUCTION

Accurate and fast measurement of the attitude of a spinning object is important for improving the accuracy of a guided projectile. Many methods can be applied to the attitude measurement of rotating objects, such as the magnetometer [1], microelectromechanical system (MEMS) inertial measurement unit (IMU) [2], global navigation satellite system (GNSS) [3], high-speed camera [4], sun sensor [5], infrared sensor [6], etc.

A magnetometer measures the attitude of an object by measuring the strength and direction of a magnetic field. A magnetometer can be employed as a specific part of a special method but is not applicable to most environments. Although MEMS gyroscopes can be utilized in normal conditions, when the angular velocity of a rotating object is very high, the attitude of the object cannot be accurately estimated due to the limited measuring range or resolution. Similarly, MEMS accelerometers measure the physical attitude by sensing the gravity vector, which is suitable in a normal environment. However, the gravity vector cannot be effectively sensed when an object is in free fall and rotates at a high speed. GNSS provides users with all-weather 3D coordinates, speed and time information at any location on the Earth's surface or in near-Earth space. However, receiving satellite information is time-consuming, performing measurements in real time is difficult, and the stability may be partially lost. High-speed cameras, sun sensors and infrared

The associate editor coordinating the review of this manuscript and approving it for publication was Xingwang Li.

sensors are excellent choices in a suitable environment but are vulnerable to a variety of environments, including the surrounding weather, in actual experiments. To obtain accurate and effective real-time measurement data, these methods are often flexibly employed in actual experiments to measure the attitude of a rotating object.

In this article, the object to be measured is usually small in size and is flying at a high speed in an extreme environment with high overload. Therefore, high-precision sensors such as gyroscopes, which are commonly employed in other experiments, are not applicable, and the attitude of the object cannot be accurately estimated. MEMS sensors with lower cost, small footprints, and high overload resistance can be used to complete measurement tasks. When measuring the attitude angle of a spinning projectile by geomagnetic sensors, ratio methods such as the three orthogonal ratio (TOR) method, crest and trough (CT) method and phase shifting ratio (PSR) method are often employed.

The TOR method is usually performed with a three-axis magnetometer and other sensors. In [7], a three-axis magnetometer and a two-axis accelerometer is used to complete an experiment. The researchers calculated the experimental data by establishing models and formulas to obtain the attitude angle of an object. However, the parameter settings of the applied model have a substantial influence on the error of the conclusion. In [8], authors combine a magneto resistive sensor and a global position system (GPS) with a mathematical model to measure the attitude angle of a flying object in real time. In [9], a three-axis magnetometer, two single-axis gyros and a GPS receiver are utilized to receive information and an integrated filter is applied to combine them. However, the strength of the GPS signal has a considerable influence on the actual measurement, and the data may be lost due to disconnection in some cases. In [10], a state estimation method for gun-launched precision projectiles using affordable technologies is presented. Navigation algorithms were developed to incorporate flight dynamic models with measurements from inertial sensors and GPS. It is also limited by GPS devices. Reference [11] is a special case, in which two magnetic sensors are nonorthogonally mounted and a mathematical expression is presented for the magnetic sensors installed at the different angles and positions. In this condition, the attitude angles are calculated by the extreme ratio of the sensor. However, the measurement scheme can only apply to the spinning projectile, which has a small varied yaw angle. In [12], a new approach to improve ballistic projectile navigation, guidance and control, which integrates hybrid attitude determination methods and gravity vector estimation method, is presented. However, the experimental system used in this method is more complicated and is more suitable for large equipment such as aircraft and missiles. Reference [13] establishes a mathematical model for a geomagnetism turns-counting sensor, and the method of calculation for an induced electromotive force was deduced in theory. This method is very susceptible to disturbing magnetic fields. In [14], a new approach for gravity vector estimations is presented and employed in an attitude determination algorithm. This method also requires a combination of multiple sensors to work together. The experimental system is complex and not suitable for small projectiles. Reference [15] provides a novel real-time detector for full attitude determination of an aerial vehicle, which is based on a tri-axis MEMS gyro, a tri-axis magnetometer and precomputed trajectory information (PTI). The Euler angles of the aerial vehicle were determined in real time. This method is only suitable for large carriers that are equipped with PTI equipment and is not suitable for small projectiles. In [16], by creating the projectile graphical model and using the results of dynamic equations for this model, pitching angle has been simulated graphically by recording the pitch attitude of the graphical model and by applying spectral filtration the rate of pitch angle at any point of the trajectory is calculated. However, determining the pitch angle of the projectile through the image requires higher experimental environment and is not widely used. A CT method is an optimized method that fully utilizes the crest and trough points of geomagnetic sensor outputs in three-orthogonal axes. According to [17], this method reduces the experimental error and improves the accuracy of the experimental results. However, the entire experimental system remains susceptible to interference, including circuits, magnetic fields, and turntables. The PSR method is represented in [18], and a magnetometer-based phase-shifting ratio method is proposed. This method does not introduce a new source of error and uses the data obtained by a sensor. However, sensor output errors and installation errors have a considerable influence on the accuracy and stability of the experimental results.

The Kalman filter (KF) is often employed in conjunction with the PSR method. A KF can better eliminate interference during an experiment and improve the accuracy of the experimental results. Extended Kalman filter (EKF) and unscented Kalman filter (UKF) are frequently used. Reference [19] presents an algorithm that employs an EKF to estimate the full attitude of a nose-controlled spin-stabilized projectile. Magnetometers and a velocity vector estimator are used to increase the computational efficiency, and a dynamic model based on the projectile equations of motion is used to analyze the predictor step of the KF. However, the parameter settings of the model have a significant influence on the measurement results. In [20], researchers design a new mixed Kalman filter that is based on an EKF and an UKF. A three-axis magnetometer sensor is embedded on the projectile, and the geomagnetic field is measured. The filter can estimate 3 attitude angles. In [21], a three-axis magnetometer sensor and a three-axis accelerometer are used to obtain geomagnetic measurements. An EKF is used to estimate three attitude angles. However, the experimental data that are disturbed in the actual experiments will produce a large error. In [22], a magnetometer and GPS are combined. Researchers present two simplified random dynamic functions and a model of the trajectory and attitude of a flying projectile. However, the instability of the GPS limits the stability of the filter.

Reference [23] derive a sigma-point Kalman filter formulation for attitude estimation, using the modified Rodrigues parameters and real data of attitude sensors. The UKF algorithm is used for attitude estimation and the gyro-based model is considered for attitude propagation. And the actual performance of the improved update method is verified through experiments. In [24], a multiplicative Kalman filter for attitude determination algorithm based on quaternions is proposed. Data are simulated using typical values for low-cost sensors, namely, 3-axes magnetometer, 3-axes gyroscope and a sun sensor. Compared with the EKF proposed for AAUSAT-3 satellite and with the QUEST method, the results indicated a better precision and low execution time. Like other solutions using solar sensors, such solutions have high requirements for the application environment. In [25], an algorithm using an EKF is presented for estimating the full attitude of a nose-controlled spin-stabilized projectile using magnetometers and a velocity vector. However, this method is greatly affected by the model, and it is prone to unstable in practical applications. In [26], A robust Kalman filter scheme is proposed to resist the influence of the outliers in the observations. Two kinds of observation error are studied, the outliers in the actual observations and the heavy-tailed distribution of the observation noise. Either of the two kinds of errors can seriously degrade the performance of the standard Kalman filter. This method can effectively improve the robustness of the filter, but it is only effective for the above two cases, and the calculation time becomes longer because the number of iterations is greatly increased.

Fading memory Kalman filter (FKF) and adaptive Kalman filter (AKF) are often used to improve the accuracy of experimental results. In [27], an KF with fading factor is derived to address the modeling errors. The proposed method has a stronger tracking ability to the true state than the standard KF in the presence of modeling errors. In [28], a new approach to adaptive estimation of multiple fading factors in the KF for navigation applications is presented, the proposed approach can significantly improve the filter performance and has the ability to restrain the filtering divergence even when system noise attributes are inaccurate. And in [29], the problem of distributed weighted robust Kalman filter fusion is studied for a class of uncertain systems with autocorrelated and cross-correlated noises. The feasibility of the method is verified by simulation. Reference [30] presents a new optimal data fusion methodology based on the adaptive fading UKF for multi-sensor nonlinear stochastic systems. Reference [31] presents an adaptive UKF with noise statistic estimator to overcome the limitation of the standard UKF. The performance of the proposed algorithm is significantly superior to the standard UKF under the condition without accurate knowledge on system noise. The method presented in [30] and [31] are only applicable to GNSS and related types of attitude measurement methods. In [32], an improved fading UKF is proposed. The new alignment algorithm performs better in terms of robustness and convergence in the condition of complex measurement noise.

Some researchers focus on the elimination of sensor errors. Reference [33] presented a design of axial 8-coils system based on Helmholtz coils, which allows to create a magnetic field with inhomogeneity is not more than 0.1% at a distance of half the radius of the geometric center of the coils system. The device corrects the magnetometer by the generated magnetic field. In [34], an offline calibration method is proposed to eliminate the errors of the sensors. The errors, which are caused by the difference in the sensor output ratio, the nonorthogonal of the sensors or constant disturbing magnetic field, are greatly suppressed. However, the most important challenge regarding geomagnetic field measurement is the interference that occurs in the working stage. Unlike accelerometers and other inertial sensors, magnetometers can be influenced at any given time and location. A structure near the sensor or a nearby power supply can cause changes in the local magnetic field. Although a careful calibration performed offline can help estimate most errors, some errors emerge only under certain conditions. For example, the power supply to a steering motor depends on the torque of the rudder, which is determined by the actual flight condition. In addition, the launch method may affect the intrinsic magnetic field of a shell, especially when using an electromagnetic launcher, which can completely change the magnetic field of the shell. Thus, an online calibration method may be better for attitude estimation when considering geomagnetic measurements. In [35], a real-time calibration method for three-axis magnetometer independent of attitude is proposed. This method presents a new model for real-time estimation and builds a new filter for parameter estimation based on the EKF. The feasibility of the method is proved by numerical simulation. However, this EKF-based implementation calibration method can not completely eliminate the influence of the interference magnetic field received during the attitude measurement process, and the final data obtained is not accurate enough, which has a certain influence on the determination of the attitude.

The core work of this paper is to eliminate the data offset caused by a disturbing magnetic field during the flying condition of a spinning projectile. An offline calibration to eliminate the sensor errors, such as those introduced in [34], is the premise of this study. For the application of geomagnetic measurement on spin stabilized projectile, compared with other filters mentioned in this paper, the filter proposed in the paper can correctly estimate the real signal at the sampling frequency of 1 kHz and signal disturbance ratio of 1. For the ratio methods based on geomagnetic measurement, the physical meaning of the signal extreme value is discussed in section II. The approximate models of both the state and the measurement are presented in section III for the KF. Simulations and a comparison are performed in section IV. The true data used as the reference for comparison is generated by a dynamics model, as discussed in subsection IV-A. The sensor's outputs and signal preprocessing are considered in subsection IV-B. A step-by-step expression of the state equations for KF is presented in subsection IV-C.

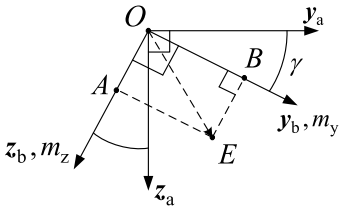

FIGURE 1. Projection of the geomagnetic field.

The algorithms of the adaptive UKF [36] [30] [32] are discussed in subsection IV-D to estimate the true geomagnetic signal and the disturbing magnetic field. The filtering results and a comparison are presented in subsection IV-E. Conclusions about the performance of the proposed filter are presented in section V.

II. GEOMETRIC INTERPRETATION OF THE RATIO METHODS

Figure 1 illustrates the process flow of the phase-shifting ratio method. In Figure 1, $\mathbf{y}_b$ and $\mathbf{z}_b$ are two coordinate axes of the body frame. The third axis of the body frame is vertically oriented into the paper and is not shown. Plane $\mathbf{y}_b\mathrm{O}\mathbf{z}_b$ is the intersecting surface of the body and is fixed in the inertial frame when both the pitch angles and yaw angles are determined. OE is the projection of the local geomagnetic field in the plane $\mathbf{y}_b\mathrm{O}\mathbf{z}_b$ and is constant if plane $\mathbf{y}_b\mathrm{O}\mathbf{z}_b$ is fixed. The symbols $\mathbf{m}_y$ and $\mathbf{m}_z$ denote the sensitive axes of the magnetic sensors along $\mathbf{y}_b$ and $\mathbf{z}_b$, respectively. OA and OB are two components of the local geomagnetic field in the body frame. Another sensor, which has a sensitive axis $\mathbf{m}_x$ along $\mathbf{x}_b$, is not shown in Figure 1.

Because OE is defined as the projection of the geomagnetic field in plane $\mathbf{y}_b\mathrm{O}\mathbf{z}_b$, further orthogonal decomposition in plane $\mathbf{y}_b\mathrm{O}\mathbf{z}_b$ should follow the rule of vector addition. Thus, the length of OE is the largest component of the geomagnetic field in plane $\mathbf{y}_b\mathrm{O}\mathbf{z}_b$.

Using the three orthogonal ratio method, when OA or OB is coaxial with OE, the extreme value is achieved, and the ratio is updated. The CT method introduces two additional update conditions. When angle AOE or BOE is equal to $\pi/4$, a simple scalar sum between OA and OB is performed, and an additional scale $sin(\pi/4)$ is applied to maintain a constant extreme value. The PSR method unites the TOR method and CT method by using a phase angle. Assuming that the extreme value is constant in one circle, the output curve of the sensor is shifted. Subsequently, the updating rate of the ratio increases and is equivalent to the sample frequency without an additional calculation cost.

All ratio methods attempt to measure or estimate the extreme value. As shown in Figure 1, however, the length of OE is the extreme value. For all ratio methods, this length is known.

First, OE is the projection of the geomagnetic field in plane $\mathbf{y}_b\mathrm{O}\mathbf{z}_b$. OE has two components in the cross-section of the body frame and can be calculated by performing direct vector addition between $\mathbf{m}_y$ and $\mathbf{m}_z$. Therefore, the determination of the extreme value is not necessary, which reduces the computational work and improves the robustness, as determining the true extreme value spot in a noisy data flow is difficult.

Second, determining the shifting angle, which is required by the PSR method, is not necessary. Assuming that the attitude angles are constant in one circle and that the extreme value is constant in the shifting process is not necessary. The length of OE can be measured at each sample time. The ratio determination and updating of the attitude angles can be performed at the same frequency.

Last, because the length of OE is the extreme value, the ratio required in these methods is the cotangent of the angle between the local geomagnetic field directions and the projectile spindle. The cotangent is inappropriate when the spindle is coaxial with the geomagnetic field directions; the sine function may instead be employed. If OC is defined as another component of the local geomagnetic field directions along the coordinate axis $\mathbf{y}_b$, the ratio can be obtained using the following:

$$r = \frac{\mathrm{OE}}{\sqrt{\mathrm{OA}^2 + \mathrm{OB}^2 + \mathrm{OC}^2}} \tag{1}$$

Similar to the equation defined in [18], equation (1) is a one-to-one monotonic function that can be utilized to determine the pitch angle. Following the remaining process of the PSR method, the attitude angles can be sequentially updated.

III. ONLINE CORRECTION BASED ON THE KALMAN FILTER

Ratio methods do not require the local geomagnetic field magnitude; however, the isotropy of sensors is crucial for determining the true attitude angles. The ratio methods and the corresponding patching rely on the realization of a calibration process before measurement. In [34], an offline calibration method was proposed, which led to a significant improvement in the sensor performance. In the paper, assuming that the error of the sensors have been eliminated, the objective of the research and the proposed filter is to correct the data dusted by the disturbing magnetic field.

The actual measurement results for online sensors can be obtained as follows:

$$(\mathbf{H}_m)_m = (\mathbf{H}_t)_m + (\mathbf{H}_r)_m \tag{2}$$

where $\mathbf{H}_t$ denotes the true value of the geomagnetic field, and $\mathbf{H}_r$ denotes the disturbing magnetic field. Symbol $()_m$ represents a projection in the measurement frame. Thus, $(\mathbf{H}_m)_m$ represents the coordinates of $\mathbf{H}_m$ in the measurement frame. $(\mathbf{H}_t)_m$ and $(\mathbf{H}_r)_m$ have similar definitions. By using the method introduced in [34], most errors that pertain to the sensors can be eliminated offline. The scales of the sensors are corrected, and the angles between the sensors are estimated. The outputs of the sensors are isotropic; however, $(\mathbf{H}_t)_m$ and $(\mathbf{H}_r)_m$ must be distinguished.

Without loss of generality, the body frame and measurement frame are coincident. Subsequently, $(\mathbf{H}_t)_m$ and $(\mathbf{H}_r)_m$

can be represented as $(\mathbf{H}_t)_b$ and $(\mathbf{H}_r)_b$, respectively. The subscript b indicates the body frame. Note that $(\mathbf{H}_t)_b$ is the product of the matrix multiplication between $\mathbf{T}_{bi}$ and $(\mathbf{H}_t)_i$. Symbol $(\mathbf{H}_t)_i$ denotes the coordinates of $\mathbf{H}_t$ in the inertial frame and is constant in certain locations. Symbol $\mathbf{T}_{bi}$ denotes the transfer matrix from the inertial frame to the body frame. Thus, $(\mathbf{H}_m)_m$ can be obtained as follows:

$$(\mathbf{H}_m)_m = \mathbf{T}_{bi}(\mathbf{H}_t)_i + (\mathbf{H}_r)_b \tag{3}$$

Both sides of (3) are differentiated with respect to time. Assuming that the disturbing magnetic field is constant or only gradually changes in the body frame, the time differential of $(\mathbf{H}_r)_b$ is regarded as zero. The attitude equations of motion are introduced, and the time differential term on $\mathbf{T}_{bi}$ is replaced. Subsequently, the time differential of $(\mathbf{H}_m)_m$ can be obtained as follows:

$$\frac{d}{dt}(\mathbf{H}_m)_m = -(\omega_b)_b^{\times}\mathbf{T}_{bi}(\mathbf{H}_t)_i \tag{4}$$

where symbol $(\omega_b)_b^{\times}$ is a three-by-three antisymmetric matrix with three independent and nonzero components according to the angular velocity. $\mathbf{T}_{bi}$ is decomposed by using the unit rotation matrix and regrouping the symbols. Thus, equation (4) can be rewritten as follows:

$$\frac{d}{dt}(\mathbf{H}_m)_m = (-(\omega_b)_b^{\times}\mathbf{T}_{\gamma})(\mathbf{T}_{\beta}\mathbf{T}_{\alpha}(\mathbf{H}_t)_i) \tag{5}$$

In (5), the term $\mathbf{T}_{\beta}\mathbf{T}_{\alpha}(\mathbf{H}_t)_i$ is OE, as shown in Figure 1; it can be regarded as a constant vector if the spindle is fixed or approximately fixed in a short time interval. If the spindle is fixed, the angular velocity in the lateral directions is zero. The first column and first row of matrix $(\omega_b)_b^{\times}$ are zero. Thus, the first column and first row of term $(\omega_b)_b^{\times}\mathbf{T}_{\gamma}$ are also zero. Consequently, the first component of $\frac{d}{dt}(\mathbf{H}_m)_m$ is zero, and the second and third components of $\frac{d}{dt}(\mathbf{H}_m)_m$ are harmonic functions. These aspects indicate that the true data for the lateral direction and axial direction are harmonic and constant, respectively.

For a spinning stabilized projectile, the angular velocity along the axis $\mathbf{x}_b$ is the main component. If the angular velocity in the lateral directions is approximately zero, the true data for the lateral directions are harmonic and can be distinguished via bias elimination. To apply the ratio method for attitude estimation, the true data for the axial directions are required. However, both the true data and the disturbing magnetic field in the axial directions are constant for a spinning projectile; thus, decoupling them.

The critical parameter for the ratio method is the angle between the spindle and the true geomagnetic field directions. If the sine function is used to estimate this angle, as indicated in (1), OC is required to calculate the length of the local geomagnetic field. However, if the sensors have been calibrated offline, the length of the local geomagnetic field is known.

The calibration method of magnetic meters, which is specified in [34], is similar to the methods that pertain to acceleration sensors. The basic concept involves fitting the sample spots on a sphere whose center is sufficiently close to the origin. Thus, the calibration has two advantages: first, the output data have an origin close to zero; second, the output data are isotropic. The first advantage enables the disturbing magnetic field in the lateral direction to be eliminated. The second advantage generates an additional property, which indicates that the length of the true local geomagnetic field is equivalent to the radius of the sphere.

Assuming that the true local geomagnetic field is not known, the angle between the spindle and the true local geomagnetic field can be calculated by dividing OE by the radius obtained based on the calibration method. Equation (1) can be represented as follows:

$$r = \frac{\mathrm{OE}}{R} \tag{6}$$

where R denotes the radius of the sphere. The advantage of (6) is the lack of OC, owing to which the data from the sensor in the spindle direction is not required.

Remark 1: The data from the sensor in the spindle direction are required in the calibration process, and thus, three sensors remain present in the body frame.

The disadvantage of (6) pertains to the associated assumption. If the magnitude of the true local geomagnetic field is known, the actual R is changed, and the ratio becomes inaccurate. The true local geomagnetic field changes with changes in the environment. The locations of the sensors and the structures surrounding the sensors can change the true local geomagnetic field. However, the variation in R caused by the difference in the locations is remarkably small within a short range and can be disregarded. The variation in R caused by the difference in location within a long range can be fixed by determining the geomagnetic field distribution. The difference between the calibration environment and the working environment has the most considerable effect on the true local geomagnetic field and R. Sensors that are calibrated in an aluminum tank will involve a significant error when deployed in a steel tank. Thus, maintaining similar calibration and working environments is important to properly employ (6). However, maintaining similar environments does not mean that calibration should be performed onsite before an actual operation. For example, a similar environment indicates that sensors working in a steel tank should be calibrated in a steel tank. Although the tanks selected for the calibration and the working conditions are not identical, they should have the same structure. The variation in the disturbing magnetic field, which is caused by shells, can be eliminated by employing bias elimination and (6).

The process of online estimation of attitude, which is based on the geomagnetic field, is shown in Figure 2.

The calibration method refers to that introduced in [34], and the attitude estimation method refers to that presented in [18].The KF is introduced to estimate the true data for the lateral directions.

Based on the discussion pertaining to (5), the true values of $(\mathbf{H}_m)_m$ in the lateral directions are two complementary

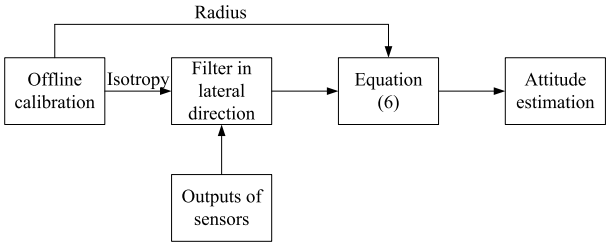

FIGURE 2. Process of online estimation.

sinusoidal signals. Thus, the state functions include the following:

$$\begin{cases} \dot{x_1} = x_3 x_2 + u_1 \\ \dot{x_2} = -x_3 x_1 + u_2 \\ \dot{x_3} = u_3 \end{cases} \tag{7}$$

where x_1 and x_2 are the outputs that correspond to the two lateral directions in the measurement frame. x_3 is a coefficient that pertains to the frequency, which is a constant when considering short periods. u_1, u_2 and u_3 indicate the state noise. Following (2), the measurement functions for the lateral directions are as follows:

$$\begin{cases} y_1 = x_1 + x_4 + v_1 \\ y_2 = x_2 + x_5 + v_2 \end{cases} \tag{8}$$

where v_1 and v_2 indicate the measurement noise. x_4 and x_5 indicate the disturbing magnetic field in the body frame (identical to that in the measurement frame); these values are also constant within a short time interval. Thus, the state functions also include the following:

$$\begin{cases} \dot{x_4} = u_4 \\ \dot{x_5} = u_5 \end{cases} \tag{9}$$

Functions (7) and (9) are total state functions. Using the measurement functions in (8), bias elimination can be performed by using the KF.

IV. EXAMPLE AND SIMULATIONS

The proposed method is developed for the measurement application in the projectile guidance kit (PGK). PGK is one kind of guidance equipment for upgrading the original unguided projectile. The keywords of the PGK are inexpensive, small and efficient. A typical PGK has a length of approximately 300 mm and a radius of approximately 30 mm. The PGK includes the rudder, fuse, central processing unit, power package, measurement system and guidance system. The rooms for sensors in the PGK are quite narrow and the interferences among different components are ordinary. For geomagnetic measurements, the outputs of the magnetometers will be disturbed by the steel shell, rudder motor, and nearby power supply wires. Some sources of the disturbance appear only on working conditions, and elimination by the celebration offline is difficult.

This section describes a simulation that was performed to validate the efficacy of the proposed method. As shown in Figure 2, the primary improvement by the new method corresponds to the phase after the offline calibration and before the attitude estimation. Neither the calibration method nor the attitude estimation methods are modified in the proposed method. If the ratio, which is the most important characteristic of all ratio methods, can be accurately estimated, the validity of the proposed method can be demonstrated.

Generally, the proposed filter should be examined by using the experiment data. However, most studies on the measurement of traditional projectiles focus on the centroid trajectory. The public data on the attitude motion of the projectiles, including the true states and the measured data, are rare. Thus, the true attitude motion of the projectile in the paper is generated by a set of attitude motion equations, which are comprehensively examined by dynamics and experiments (refer to subsection IV-A). The measured data that are used to feed the proposed filter are calculated by the process described in subsection IV-B. The functions for one-step state prediction of the KF are presented in subsection IV-C. The corrections for the filtering method are presented in subsection IV-D. The filtering results are presented and compared in subsection IV-E.

A. MODEL AND THE ATTITUDE MOTION

The kinetic model of the spinning object can be defined as follows:

$$(\dot{\omega_b})_b = (\mathbf{I})_b^{-1}[(\mathbf{M})_b - (\omega_b)_b^{\times}(\mathbf{I})_b(\omega_b)_b] \tag{10}$$

where $\mathbf{I}$ denotes the inertia tensor, and $\mathbf{M}$ denotes the moment of force. The kinematic equation can be presented as follows:

$$\dot{\mathbf{Q}} = \frac{1}{2}\begin{bmatrix} 0 & -(\omega_b)_b^{\mathrm{T}} \\ (\omega_b)_b & -(\omega_b)_b^{\times} \end{bmatrix}\mathbf{Q} \tag{11}$$

where $\mathbf{Q}$ is a rotation quaternion, and the yaw angle ψ, pitch angle θ and roll angle ϕ can be defined using the elements of $\mathbf{Q}$ as follows:

$$\begin{cases} \psi = \arctan\left(\dfrac{2(q_1q_2 + q_0q_3)}{1 - 2(q_2^2 + q_3^2)}\right) \\ \theta = \arcsin\left(-2(q_1q_3 - q_0q_2)\right) \\ \phi = \arctan\left(\dfrac{2(q_0q_1 + q_2q_3)}{1 - 2(q_1^2 + q_2^2)}\right) \end{cases} \tag{12}$$

As defined in [37], the moment of force can be expressed as follows:

$$\begin{aligned} (\mathbf{M})_b = {} & \frac{\Delta}{\sin(\Delta)}[a\,|\mathbf{V}|\,(\mathbf{V})_b \times (\mathbf{x}_b)_b \\ & + d\omega_{bx}(\mathbf{x}_b)_b \times ((\mathbf{x}_b)_b \times (\mathbf{V})_b)] \\ & - |\mathbf{V}|\begin{bmatrix} c & 0 & 0 \\ 0 & b & 0 \\ 0 & 0 & b \end{bmatrix}(\omega_b)_b \end{aligned} \tag{13}$$

where a, b, c and d are the coefficients of turning torque, lateral damping, rolling damping, and Magnus moment, respectively. Δ is the total angle of attack. In an appropriate initial condition, all attitude angles can be calculated by

TABLE 1. The coefficients used by the model.

Parameter		Value
Moment of inertia in the body frame	x	$0.16\ (\mathrm{kg}\cdot\mathrm{m}^2)$
	y	$1.8\ (\mathrm{kg}\cdot\mathrm{m}^2)$
	z	$1.8\ (\mathrm{kg}\cdot\mathrm{m}^2)$
Product of inertia in the body frame		All zeros
Coefficient that correspond to the torque	a	$10^{-4}\ (\mathrm{N}\cdot\mathrm{s}^2/\mathrm{m}^2)$
	b	$10^{-4}\ (\mathrm{N}\cdot\mathrm{s}^2/\mathrm{m})$
	c	$5\times10^{-6}\ (\mathrm{N}\cdot\mathrm{s}^2/\mathrm{m})$
	d	$10^{-6}\ (\mathrm{N}\cdot\mathrm{s}^2/\mathrm{m})$
Initial angular velocity in the body frame	x	$400\pi\ (\mathrm{Rad/s})$
	y	$0.1\ (\mathrm{Rad/s})$
	z	$0\ (\mathrm{Rad/s})$
Initial attitude angle	ψ	$0.01\ (\mathrm{Rad})$
	θ	$0.01\ (\mathrm{Rad})$
	ϕ	$0\ (\mathrm{Rad})$
Initial inflow velocity in the inertia frame	x	$1000\ (\mathrm{m/s})$
	y	$0\ (\mathrm{m/s})$
	z	$0\ (\mathrm{m/s})$

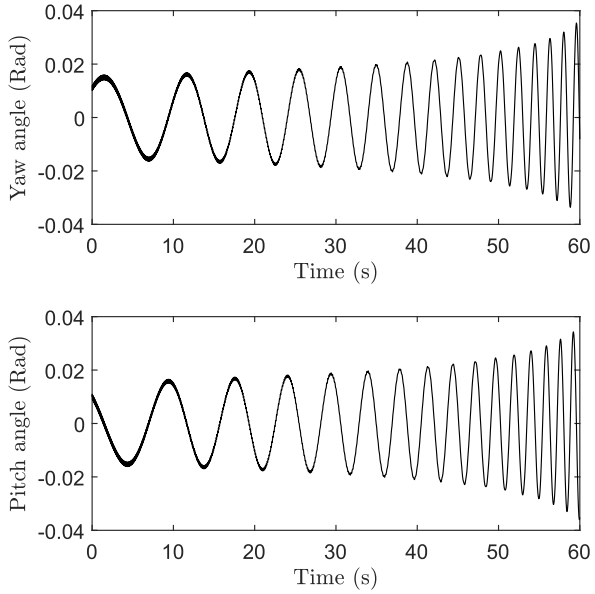

FIGURE 3. Time history of attitude movement.

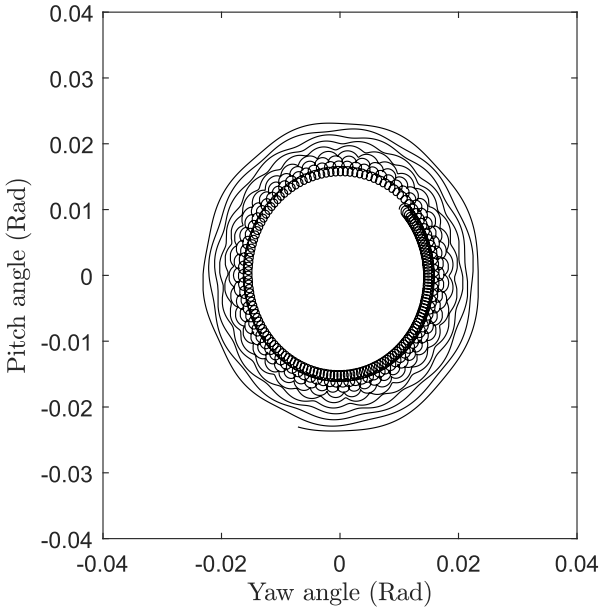

FIGURE 4. Attitude movement of the spinning object.

solving (10), (11) and (13). The results obtained using these equations are regarded as the true values that pertain to the attitude movement. The coefficients in (10), (11) and (13) are listed in Table 1.

Remark 2: The parameters listed in Table 1 are selected to ensure that the movement of the object is practical and reasonable. All values of the parameters can be adjusted to adapt to a certain application.

The attitude angles of the spin object that are calculated using the parameters listed in Table 1 are shown in Figure 3 and Figure 4. Only the yaw angle and the pitch angle, which are important for the spindle's movement, are determined.

Figure 3 presents the time history of the yaw angle and the pitch angle. On a larger time scale, both plots are harmonic-like with frequencies that increase with time. On a smaller time scale, both the yaw angle and the pitch angle are shaking and the amplitudes decrease with time. By dynamics, the motion produced when the spindle revolves around the direction of initial angular velocity is referred to as the procession; the motion produced when the spindle near or far from the direction of initial angular velocity is referred to as the nutation. When the rolling angular velocity is decreased by the rolling damping, the orientation of the spinning object is weakened and the nutation angle increases. For a flying object, the turning torque and the angular velocity of procession will increase. The shake of the nutation is caused by the initial conditions. When the actual angular velocity of the spindle is not equal to the angular velocity governed by (10), additional angular displacement causes oscillation of the spindle. However, the lateral damping will damp the shaking energy, which explains why the amplitudes will decrease. Figure 4 presents a clear graph of the relationship between the yaw angle and the pitch angle. The spindle starts from the inside circle and rotates clockwise. Note that the procession is quite slow, only two complete cycles during a period of twenty seconds.

Compared with the real attitude motion of flying projectiles, the attitude motion generated by the model may exhibit several differences. First, the centroid motion is disregarded; thus, gravitational bending of the trajectory is also disregarded. Additional attitude deflections, which cause ballistic drift, are not shown in Figure 3 and Figure 4. Second, in real flying conditions, the vertical axis of a stabilizing projectile will follow the direction of the centroid velocity. Because the trajectory is bending, the center of the procession will move downward in Figure 4. Third, equation (13) uses a set of linear coefficients to represent the aerodynamic force on the projectile. The nonlinear aerodynamic effect is not directly reflected. For a flying object with a simple shape and a small angle of attack, linearized aerodynamic forces are generally acceptable.

According to the analysis in section III, the center of the sensors outputs is not offset; although the length of OE

may change. The ballistic drift and the deflection velocity of the vertical axis are very slow processes. Filters that correctly process the data shown in Figure 3 can adapt to real data processing. For a flying object with a simple shape and a small angle of attack, linearized aerodynamic forces are generally acceptable. If necessary, these coefficients can be substituted for a combination of air density and velocity to accommodate changes in altitude, humidity, and velocity.

B. SENSOR'S OUTPUTS AND SIGNAL PREPROCESSING

In practice, sensor performance will be slightly different, and the sensors may be incorrectly installed. Calibration is a necessary task to eliminate installation errors and compensate for sensor performance. In this paper, the calibration process is assumed to be perfect, and the sensor data have been correctly converted to the measurement frame.

For each sampling time, the sensor output d_{so} is physically scaled to $(\mathbf{H}_{\mathrm{m}})_{\mathrm{m}}$ and is presented as follows:

$$d_{\mathrm{so}} = r_{\mathrm{s}} \left(\mathbf{H}_{\mathrm{m}}\right)_{\mathrm{m}} \tag{14}$$

where r_{s} is the output ratio of the sensor. The sensor output d_{so} should be scaled to the range of the adaptive analog-to-digital (AD) converter. Consider the disturbing magnetic field; to avoid losing information, the factor should be carefully selected. Assuming that the amplifier is ideal, the amplification coefficient c_{a} should balance the equation as follows:

$$c_{\mathrm{a}} V_{\mathrm{ppdso}} = r_{\mathrm{fs}} V_{\mathrm{fs}} \tag{15}$$

where r_{fs} is the utilization of full scale and is selected as 0.9 to reduce nonlinear distortion; V_{fs} is the input voltage range of the AD converter; and V_{ppdso} is the peak-to-peak value of d_{so}. Assuming that the AD converter is ideal, the sampling process of the AD converter is simulated by using a function that rounds a number to the nearest integer. The data obtained after the AD converter is presented as follows:

$$d_{\mathrm{ad}} = round\left(\frac{2^{n_{\mathrm{ad}}}}{V_{\mathrm{fs}}} c_{\mathrm{a}} d_{\mathrm{so}}\right) \tag{16}$$

where n_{ad} is the bit number of an AD converter. Substituting (14) and (15) into (16), d_{ad} can be represented as follows:

$$d_{\mathrm{ad}} = round\left(2^{n_{\mathrm{ad}}} \frac{r_{\mathrm{fs}}}{V_{\mathrm{ppdso}}} r_{\mathrm{s}} (\mathbf{H}_{\mathrm{m}})_{\mathrm{m}}\right) \tag{17}$$

Similar to the data supported by the AD converter in practice, the elements of d_{ad} are integers. To simplify the expression of the filtering process, the integers are divided by the full scale of the AD converter. Most on-chip applications can only perform single-precision floating-point calculations. Thus, the results of this division should be restricted to single precision. This operation can be achieved by using the *single*() function for MATLAB or single-precision data type casts for a C compiler. The data prepared for the filter is presented as follows:

$$d_{\mathrm{pre}} = single\left(\frac{d_{\mathrm{ad}}}{2^{n_{\mathrm{ad}}-1}}\right) \tag{18}$$

To complete the data preparation, $(\mathbf{H}_{\mathrm{m}})_{\mathrm{m}}$ should be specific. According to (3), the other three variables– $(\mathbf{H}_{\mathrm{t}})_{\mathrm{i}}$, $\mathbf{T}_{\mathrm{bi}}$ and $(\mathbf{H}_{\mathrm{r}})_{\mathrm{b}}$–need to be determined.

$(\mathbf{H}_{\mathrm{t}})_{\mathrm{i}}$ can be calculated by the geomagnetic declination ψ_{geo}, geomagnetic inclination θ_{geo} and magnitude of the geomagnetic $|\mathbf{H}_{\mathrm{t}}|$; they are determined as initial condition and in frame of north east down (NED), and the direction of $\mathbf{H}_{\mathrm{t}}$ is presented as follows:

$$\left(\vec{\mathbf{H}}_{\mathrm{t}}\right)_{\mathrm{i}} = \begin{bmatrix} cos(\theta_{\mathrm{geo}})cos(\psi_{\mathrm{geo}}) \\ cos(\theta_{\mathrm{geo}})sin(\psi_{\mathrm{geo}}) \\ sin(\theta_{\mathrm{geo}}) \end{bmatrix} \tag{19}$$

According to the model presented in subsection IV-A, the transform matrix $\mathbf{T}_{\mathrm{bi}}$ in (3) can be calculated by the rotation quaternion and is expressed as follows:

$$\mathbf{T}_{\mathrm{bi}} = \mathbf{q}\mathbf{q}^{\mathrm{T}} + \left(q_0 \mathbf{I}_{3\times 3} - \mathbf{q}^{\times}\right)^2 \tag{20}$$

where q_0 and $\mathbf{q}$ is the scale part and the vector part, respectively, of rotation quaternion $\mathbf{Q}$; $\mathbf{I}_{3\times 3}$ is a unit matrix with dimension 3×3.

For $(\mathbf{H}_{\mathrm{r}})_{\mathrm{b}}$, two kind of interferences are considered in the subsection. The first interference is caused by nearby disturbing magnetic fields, such as the intrinsic magnetic field of the shell. This kind of interference slowly changes in the body frame and is modeled as a bias of the outputs data. The size of the bias conforms to a uniform distribution. The second interference is the thermal noise of the sensor and is modeled as white Gaussian noise. Both disturbances have zero mean and are superimposed on the sensor output by addition. Thus, $(\mathbf{H}_{\mathrm{r}})_{\mathrm{b}}$ can be presented as follows:

$$(\mathbf{H}_{\mathrm{r}})_{\mathrm{b}} = \delta_{\mathrm{G}} \mathbf{G} + r_{\mathrm{U}} \frac{\mathbf{U}}{|\mathbf{U}|} \tag{21}$$

where both $\mathbf{G}$ and $\mathbf{U}$ are vectors with three elements; each element of $\mathbf{G}$ is generated by a standard Gaussian distribution; each element of $\mathbf{U}$ is generated by a standard uniform distribution with zero mean; δ_{G} is the variance of the normal distribution; the fraction in (21) converts $\mathbf{U}$ to a unit vector; and r_{U} is the length of the random vector.

By substituting (21) into (3), $(\mathbf{H}_{\mathrm{m}})_{\mathrm{m}}$ can be represented as follows:

$$(\mathbf{H}_{\mathrm{m}})_{\mathrm{m}} = \left[\mathbf{T}_{\mathrm{bi}} \left(\vec{\mathbf{H}}_{\mathrm{t}}\right)_{\mathrm{i}} + \frac{1}{r_{\mathrm{sd}}} \frac{\mathbf{U}}{|\mathbf{U}|} + \frac{1}{r_{\mathrm{sn}}} \mathbf{G}\right] |\mathbf{H}_{\mathrm{t}}| \tag{22}$$

where $(\mathbf{H}_{\mathrm{t}})_{\mathrm{i}}$ is decomposed by $|\mathbf{H}_{\mathrm{t}}|$ and a unit vector $\vec{\mathbf{H}}_{\mathrm{t}}$ which represents the direction of the geomagnetic vector; symbol r_{sd} is defined as $|\mathbf{H}_{\mathrm{t}}|$ to the r_{U} ratio; and symbol r_{sn} is defined as δ_{G} to the $|\mathbf{H}_{\mathrm{t}}|$ ratio. r_{sd} and r_{sn} can be presented as follows:

$$r_{\mathrm{sd}} = \frac{|\mathbf{H}_{\mathrm{t}}|}{r_{\mathrm{U}}} \tag{23}$$

$$r_{\mathrm{sn}} = \frac{|\mathbf{H}_{\mathrm{t}}|}{\delta_{\mathrm{G}}} \tag{24}$$

Generally, r_{sn} is a large number; thus, the length of $\mathbf{G}/r_{\mathrm{sn}}$ is a small number and is disregarded. $\mathbf{T}_{\mathrm{bi}}(\vec{\mathbf{H}}_{\mathrm{t}})_{\mathrm{i}}$ is a unit vector.

TABLE 2. Parameters and initial values.

Symbol	Quantity	Values
Δt	Sample interval	$10^{-3}(s)$
ψ_{geo}	Geomagnetic declination according to inertial frame	$\pi/4(\text{Rad})$
θ_{geo}	Geomagnetic inclination according to inertial frame	$\pi/4(\text{Rad})$
$\lvert\mathbf{H}_{\text{t}}\rvert$	The magnitude of the geomagnetic	1
n_{ad}	Bit number of an AD converter	16
r_{fs}	The utilization of full scale	0.9
r_{sd}	$\lvert\mathbf{H}_{\text{t}}\rvert$ to r_{U} ratio	1
r_{sn}	δ_{G} to $\lvert\mathbf{H}_{\text{t}}\rvert$ ratio	20

The maximum length of the vector bounded by square brackets in (22) is approximately equal to $1 + r_{\text{sd}}^{-1}$, and V_{ppdso} can be presented as follows:

$$V_{\text{ppdso}} = 2\left(1 + r_{\text{sd}}^{-1}\right) r_{\text{s}} \left|\mathbf{H}_{\text{t}}\right| \tag{25}$$

By substituting (22) and (25) into (17), d_{ad} is represented as follows:

$$d_{\text{ad}} = round\left(2^{n_{\text{ad}}-1} \frac{r_{\text{fs}} r_{\text{sd}}}{1 + r_{\text{sd}}} \left[\mathbf{T}_{\text{bi}} \left(\vec{\mathbf{H}}_{\text{t}}\right)_{\text{i}} + \frac{1}{r_{\text{sd}}} \frac{\mathbf{U}}{|\mathbf{U}|} + \frac{1}{r_{\text{sn}}} \mathbf{G}\right]\right) \tag{26}$$

Equation (26) indicated that the data collected after AD converter in the simulation depends only on the direction of the geomagnetic vector and is not related to the magnitude of the geomagnetic vector. Thus, the process of the measurement simulation can start with a unit geomagnetic vector, whose direction is presented in (19). Equation (26) also gains thermal noise. The larger is the parameter r_{sd}, which represents the signal-to-disturbance ratio in this paper, acts as a coefficient in allocating the proportion of useful signals and disturbance signals in the data. A large r_{sd} increases the proportion of useful signals in the data. For an AD conversion process of limited depth, a larger number of bits is used to record valid data, and the resolution of valid data is improved. The parameter r_{sd} also gains the thermal noise. The larger the parameter r_{sd}, the greater is the noise gain. Thus, for a smaller r_{sd}, the data to be processed will contain a large state disturbance and a small random noise. For a larger r_{sd}, the opposite is true. The influence of r_{sd} on the filtering results is presented in subsection IV-E.

The process of generating the simulated measurement data at each sampling time is listed as follows: 1) Set the initial values; 2) Calculate the rotation quaternion at certain sampling times by (10), (11) and (13); 3) Calculate $(\vec{\mathbf{H}}_{\text{t}})_{\text{i}}$ by (19); 4) Calculate $\mathbf{T}_{\text{bi}}$ by (20); 5) Calculate d_{ad} by (26); 6) The data prepared for the filters are achieved by (18).

The parameters and initial values in this process are listed in Table 2. Figure 5 shows the theoretical truth values of $(\vec{\mathbf{H}}_{\text{t}})_{\text{b}}$ before amplification and sampling. The sampling process requires 60 seconds, and the sampling frequency is 1 kHz. The first subplot in 5 presents the component of $(\vec{\mathbf{H}}_{\text{t}})_{\text{b}}$ along $\mathbf{x}_{\text{b}}$. The value slightly fluctuated near 0.5. The low-frequency fluctuation and high-frequency fluctuation reflect the precession and nutation, respectively, of the projectile. The second

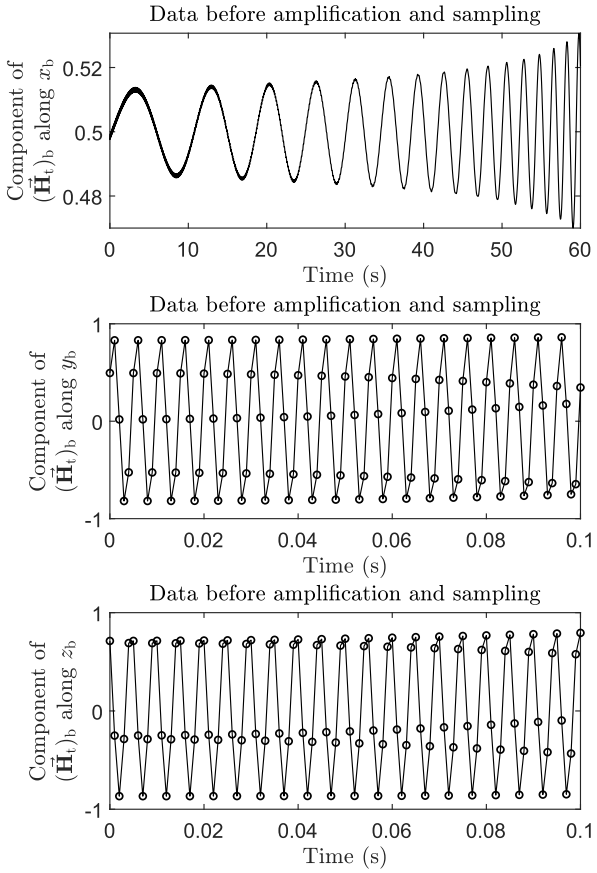

FIGURE 5. True data at each sample time before amplification and sampling.

subplot and third subplot in Figure 5 present the component of $(\vec{\mathbf{H}}_{\text{t}})_{\text{b}}$ along $\mathbf{y}_{\text{b}}$ and $\mathbf{z}_{\text{b}}$, respectively. The horizontal axes of the graphs are restricted between 0 seconds and 0.1 seconds for clean viewing. For a rolling motion with a frequency of 200 Hz, the sampling frequency of 1 kHz is not high, which is one of the difficulties of the attitude measurement of high-rotation objects.

Figure 6 shows the data given by the simulated measurement process before the last step. The disturbance is randomly shifted every 6 seconds, and the SDR is set to 1. Compared with Figure 6, the data shown in Figure 6 is highly disturbed. Additional magnetic interference causes the data to be deflected. If the data in Figure 6 were directly applied to calculate the ratio in the ratio methods, the correct results would not be obtained. Because SDR is set to 1, the maximum length of the vector in the square bracket is approximately 2 in (26). To adapt to the range of the AD converter, the amplification gain is relatively increased; thus, useful signals, including thermal noise are greatly amplified. The magnification ratio increases when the SDR increases; and decreases when the SDR decreases. The low amplification ratio reduces the useful information acquired by the AD converter, which will affect the filtering quality. In subsection IV-E, additional conclusions will be presented based on comparison of the filtering results.

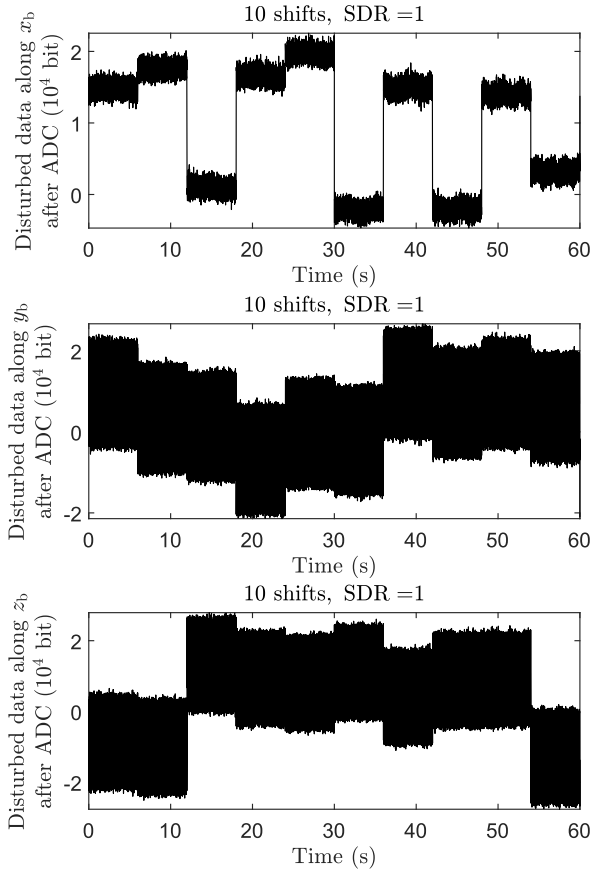

FIGURE 6. Disturbed data.

C. FUNCTIONS FOR ONE-STEP STATE PREDICTION

Equations (7) and (9) are continuity equations. To apply the KF using discrete data in practice, the discrete form of the state equations is required. As shown in (7) and (9), if x_3 is constant within a short period, the integration of the differential equations with respect to x_1 and x_2 can be determined. In this situation, the state variables x_1 and x_2 can be presented as follows:

$$\begin{cases} x_1 = Asin(x_3 t + \omega_0) \\ x_2 = Acos(x_3 t + \omega_0) \end{cases} \tag{27}$$

where A denotes the amplitude, and ω_0 denotes the phase position. Both A and ω_0 can be determined using the initial conditions. Thus, at both instants t_k and t_{k+1}, equation (27) generates the following two sets of equations:

$$\begin{cases} x_1(k) = Asin(x_3(k)t_k + \omega_0) \\ x_2(k) = Acos(x_3(k)t_k + \omega_0) \end{cases} \tag{28}$$

and

$$\begin{cases} x_1(k+1) = Asin(x_3(k)t_{k+1} + \omega_0) \\ x_2(k+1) = Acos(x_3(k)t_{k+1} + \omega_0) \end{cases} \tag{29}$$

In (29), t_{k+1} represents the sum of t_k and Δt. Δt is a constant and denotes the sample interval. Thus, the trigonometric functions on the right-hand side of (29) can be expanded by the factors $sin(x_3\Delta t)$ and $cos(x_3\Delta t)$ and simplified using (28) as follows:

$$\begin{cases} x_1(k+1) = x_1(k)cos(x_3(k)\Delta t) + x_2(k)sin(x_3(k)\Delta t) \\ x_2(k+1) = x_2(k)cos(x_3(k)\Delta t) - x_1(k)sin(x_3(k)\Delta t) \end{cases} \tag{30}$$

The amplitude and phase position are not required in (30). Thus, equations (30) can be applied for other conditions in which the magnitude of the local geomagnetic field is not one. In (30), x_3 is the rolling angle velocity and its value is considerable larger than other state variables in this case. To ensure that all state variables have the same order of magnitude, x_3 is reformulated as a product of a constant and a scale. Equation (30) can be represented as follows:

$$\begin{cases} x_1(k+1) = x_1(k)cos(\omega e^{x_3(k)}\Delta t) + x_2(k)sin(\omega e^{x_3(k)}\Delta t) \\ x_2(k+1) = x_2(k)cos(\omega e^{x_3(k)}\Delta t) - x_1(k)sin(\omega e^{x_3(k)}\Delta t) \end{cases} \tag{31}$$

where ω is a constant and can be determined by experience or estimation. For example, the selection of ω of approximately 400π for a typical projectile is reasonable. $e^{x_3(k)}$ acts as the scale of ω. The exponent function is selected to ensure that the scale is always larger than zero, which is important to ensure the stability of the filter.

The discrete forms of the remaining state variable are as follows:

$$\begin{cases} x_3(k+1) = x_3(k) \\ x_4(k+1) = x_4(k) \\ x_5(k+1) = x_5(k) \end{cases} \tag{32}$$

Equations (31) and (32) are used to perform the one-step state prediction for the KF.

D. ALGORITHM IMPROVEMENT

KF has a long history. UKF is extensively applied because it can better address nonlinear problems. The classical UKF has the disadvantages of slow convergence, small time step required, and long-term errors. Recently, some researchers have developed some new methods to overcome the shortcomings of UKF.

Deng *et a.* [36] developed a new adaptive robust UKF (AUKF) scheme that is referred to as adaptive maximum correntropy UKF (AMUKF), which is based on both a fading factor and the maximum correntropy criterion (MCC). Compared with other existing KFs, the proposed filter has a better adaptive ability to balance the contribution between the process model information and the measurements of the state variables. The AMUKF can also retain the effect of outliers. The AMUKF is simple and easily implemented on the chip. However, some points need to be clarified. Although in [36] may include a clerical error, a consistent description of the specific steps of the AMUKF is not avaliable, such as the discussion of the sigma points used in state prediction and measurement prediction. Generally, if two images of different mappings are compared, the correct result can be obtained only by using the same preimage. In each step

TABLE 3. Algorithm of AMUKF in *k*th loop.

1) Sigma points update. x_{k-1} and P_{k-1} are used to update the sigma points. A detailed description of the sigma points update method refers to [40]. The parameters $w_{\mathrm{m},i}$ and $w_{\mathrm{c},i}$ in the following steps are the mean weighted coefficient and the variance weighted coefficient, respectively. These parameters differ and are determined by the sigma points update process.
2) Time update.
$\hat{x}_i = f(\chi_i)$
$\bar{x} = \sum_{i=0}^{2n} w_{\mathrm{m},i}\hat{x}_i$, the symbol n represents the number of the state variables.
3) Measurement update.
$\hat{y}_i = h(\hat{x}_i)$
$\bar{y} = \sum_{i=0}^{2n} w_{\mathrm{m},i}\hat{y}_i$
$\hat{P}_{\mathrm{yy}} = \sum_{i=0}^{2n} w_{\mathrm{c},i}\left(\hat{y}_i - \bar{y}\right)\left(\hat{y}_i - \bar{y}\right)^{\mathrm{T}} + P_{\mathrm{w}}$
4) Calculate the factor. The updating process of the factor is identical to that in [36]. The symbol y_k represents the measurement data for the kth loop.
$v = y_k - \bar{y}$
$C_k = \begin{cases} vv^{\mathrm{T}}, k = 1 \\ (\lambda C_{k-1} + vv^{\mathrm{T}})/(1+\lambda), k > 1 \end{cases}$
$c_0 = tr(C_k - P_{\mathrm{w}})/tr(\hat{P}_{\mathrm{yy}} - P_{\mathrm{w}})$, the symbol P_{w} represents the initial measurement variance
$c = \begin{cases} c_0, c_0 > 1 \\ 1, c_0 \le 1 \end{cases}$
5) Kalman Update.
$\hat{P}_{\mathrm{xx}} = c\left[\sum_{i=0}^{2n} w_{\mathrm{c},i}\left(\hat{x}_i - \bar{x}\right)\left(\hat{x}_i - \bar{x}\right)^{\mathrm{T}} + P_{\mathrm{v}}\right]$, the symbol P_{v} represents the initial state variance.
$P_{\mathrm{xy}} = c\sum_{i=0}^{2n} w_{\mathrm{c},i}\left(\hat{x}_i - \bar{x}\right)\left(\hat{y}_i - \bar{y}\right)^{\mathrm{T}}$
$P_{\mathrm{yy}} = c\hat{P}_{\mathrm{yy}} + (1-c)P_{\mathrm{w}}$
$K = P_{\mathrm{xy}}P_{\mathrm{yy}}^{-1}$
$x_k = \bar{x} + Kv$
$P_k = \hat{P}_{\mathrm{xx}} - KP_{\mathrm{yy}}K^{\mathrm{T}}$

of the KF, the update of an observation is based on the prediction of a state. Although the state equations and the measuring equations are usually separately expressed, equations should be linked and the same preimage should be used. If $x_{k+1} = f(x_k)$ is the state equation and $h(x_{k+1})$ is the measuring equation, an unscented transformation (UT) will be performed by calculating $f(\chi_i)$ and $h(f(\chi_i))$, where the symbol χ_i denotes the ith sigma point. The relevant steps have been clearly described in previous studies [38]. In this subsection, the basic process of UKF will follow [38]. The algorithm of the AMUKF in the kth loop is represented in Table 3.

In Table 3, all variables with the subscript k need to be cached for the next loop, with the exception of y_k. By AMUKF, the factor c is also applied to P_{xy} and P_{w}. Because the Kalman gain K is calculated by $P_{\mathrm{xy}}P_{\mathrm{yy}}^{-1}$, the factor c affect K. By the AMUKF, the state variables will quickly converge to the measurements. However, if the measured data is extremely noisy, the filter may lose its stability.

In other studies [30] [32], the factor c is only applied to $\hat{P}_{\mathrm{xx}}$. However, the literature claims that the modification of the algorithm is based on the UKF using UT twice in each loop. The algorithm in the kth loop is represented in Table 4. To distinguish the algorithm listed in Table 4, this algorithm is designate "AUKF1" in the paper. Since the calculation process of the Kalman gain is not modified, the Kalman gain will remain stable with noisy data. The performance of AUKF1 is included in the following comparison.

TABLE 4. Algorithm of AUKF1 in *k*th loop.

1) Sigma points update.
2) Time update.
$\hat{x}_i = f(\chi_i)$
$\bar{x} = \sum_{i=0}^{2n} w_{\mathrm{m},i}\hat{x}_i$
$\hat{P}_{\mathrm{xx}} = \sum_{i=0}^{2n} w_{\mathrm{c},i}\left(\hat{x}_i - \bar{x}\right)\left(\hat{x}_i - \bar{x}\right)^{\mathrm{T}} + P_{\mathrm{v}}$
3) Sigma points update at $\bar{x}$ with $\hat{P}_{\mathrm{xx}}$; $\hat{\chi}_i$ indicates the new sigma points.
4) Measurement update.
$\hat{y}_i = h(\hat{\chi}_i)$
$\bar{y} = \sum_{i=0}^{2n} w_{\mathrm{m},i}\hat{y}_i$
$\hat{P}_{\mathrm{yy}} = \sum_{i=0}^{2n} w_{\mathrm{c},i}\left(\hat{y}_i - \bar{y}\right)\left(\hat{y}_i - \bar{y}\right)^{\mathrm{T}} + P_{\mathrm{w}}$
5) Calculate the factor.
$v = y_k - \bar{y}$
$C_k = \begin{cases} vv^{\mathrm{T}}, k = 1 \\ (\lambda C_{k-1} + vv^{\mathrm{T}})/(1+\lambda), k > 1 \end{cases}$
$c_0 = tr(C_k - P_{\mathrm{w}})/tr(\hat{P}_{\mathrm{yy}} - P_{\mathrm{w}})$
$c = \begin{cases} c_0, c_0 > 1 \\ 1, c_0 \le 1 \end{cases}$
6) Kalman update.
$P_{\mathrm{xx}} = c\hat{P}_{\mathrm{xx}}$
$P_{\mathrm{xy}} = \sum_{i=0}^{2n} w_{\mathrm{c},i}\left(\hat{x}_i - \bar{x}\right)\left(\hat{y}_i - \bar{y}\right)^{\mathrm{T}}$
$K = P_{\mathrm{xy}}P_{\mathrm{yy}}^{-1}$
$x_k = \bar{x} + Kv$
$P_k = \hat{P}_{\mathrm{xx}} - KP_{\mathrm{yy}}K^{\mathrm{T}}$

TABLE 5. Algorithm of AUKF2 in *k*th loop.

1) Sigma points update.
2) Time update.
$\hat{x}_i = f(\chi_i)$
$\bar{x} = \sum_{i=0}^{2n} w_{\mathrm{m},i}\hat{x}_i$
3) Measurement update.
$\hat{y}_i = h(\hat{x}_i)$
$\bar{y} = \sum_{i=0}^{2n} w_{\mathrm{m},i}\hat{y}_i$
$P_{\mathrm{yy}} = \sum_{i=0}^{2n} w_{\mathrm{c},i}\left(\hat{y}_i - \bar{y}\right)\left(\hat{y}_i - \bar{y}\right)^{\mathrm{T}} + P_{\mathrm{w}}$
4) Calculate the factor.
$v = y_k - \bar{y}$
$C_k = \begin{cases} v^{\mathrm{T}}v, k = 1 \\ (\lambda C_{k-1} + v^{\mathrm{T}}v)/(1+\lambda), k > 1 \end{cases}$
$c_0 = \left(C_k - tr(P_{\mathrm{w}})\right)/tr(\hat{P}_{\mathrm{yy}} - P_{\mathrm{w}})$
$c = \begin{cases} c_0, c_0 > 1 \\ 1, c_0 \le 1 \end{cases}$
5) Kalman update.
$P_{\mathrm{xx}} = c\left[\sum_{i=0}^{2n} w_{\mathrm{c},i}\left(\hat{x}_i - \bar{x}\right)\left(\hat{x}_i - \bar{x}\right)^{\mathrm{T}} + P_{\mathrm{v}}\right]$
$P_{\mathrm{xy}} = \sum_{i=0}^{2n} w_{\mathrm{c},i}\left(\hat{x}_i - \bar{x}\right)\left(\hat{y}_i - \bar{y}\right)^{\mathrm{T}}$
$P_{\mathrm{yy}} = \sum_{i=0}^{2n} w_{\mathrm{c},i}\left(\hat{y}_i - \bar{y}\right)\left(\hat{y}_i - \bar{y}\right)^{\mathrm{T}} + P_{\mathrm{w}}$
$K = P_{\mathrm{xy}}P_{\mathrm{yy}}^{-1}$
$x_k = \bar{x} + Kv$
$P_k = P_{\mathrm{xx}} - KP_{\mathrm{yy}}K^{\mathrm{T}}$

For comparison, the adaptive filtering method that is utilized only once with sigma points. The update process is described in Table 5 and designated as "AUKF2". Most of the steps in AUKF2 are identical to those in AUKF1, with the exception that the variable $\hat{y}_i$ is calculated by $\hat{x}_i$ instead of by $\hat{\chi}_i$. Notice the variable C_k in the Table 5 is calculated and updated by the inner product of innovation vector. And the fraction used to calculate variable c_0 is also revised. This is because that the trace of the matrix is equal to the sum of the main elements. And the main elements of matrix C_k are square of innovation vector elements by sequential. Thus, the trace of the matrix C_k is equal to the inner product of innovation vector. The revise on C_k and c_0 in Table 5

TABLE 6. Parameters that are commonly employed by two sets of simulation.

Parameter		Value
Parameters for unscented transform	α	10^{-3}
	μ	9×10^{-3}
	β	2
	κ	-2
Initial values of state variables	x_1	1
	x_2	0
	x_3	0
	x_4	0
	x_5	0
Initial covariance matrix of state variables	Diagonal	All ones
	Others	All zeros
Initial covariance matrix of process noise	Principal elements (10^{-3})	0.5 0.5 2 5 5
	Others	All zeros
Initial covariance matrix of measurement noise	Diagonal	All 2.5×10^{-4}
	Others	All zeros
Estimate of rolling angle velocity in the state model		350π (Rad/s)
Sample interval		10^{-3} (s)
λ		300

can reduce the calculating costs and save the memory for on-chip system. All algorithms listed in Table 3, Table 4 and Table 5 will be compared in the next subsection using the same parameters.

E. SIMULATION AND THE RESULTS

In this subsection, different UKF algorithms are used to correct the sensor's output. Two sets of simulations are performed. In the first set of simulations, the SDR is equal to one, and the performance of the UKF algorithms is compared. In the second set of simulations the adaptability of the algorithms to state disturbances and noise is discussed by changing the SDR.

The parameters that are commonly employed by the two sets of simulations are listed in Table 6. A comparison of Table 6 to Table 1 and Table 2 reveals that some initial conditions and parameters are biased and inaccurate.

Remark 3: The value of those initial covariance matrixes will affect the outputs of the filters. However, the statistical characteristics of process and measurement noise cannot be fully determined in practice. Dynamic adaptation and correction of those statistical characteristics are the research direction of adaptive KF, but not the objective of this paper. Those initial matrixes in Table 6 can ensure the operation of the filters and are not optimized. According to the specific noise characteristic used in the simulation, there may be other values of those covariance matrixes to make the output of the filter better.

The classic UKF, AMUKF (designated as "AUKF"), AUKF1 and AUKF2 are compared in this subsection. The OE calculated by using the data before filtering and the OE calculated by using the data after filtering are compared. The simulation requires 60 seconds, and the SDR is equal to one. The results and the comparison are shown in

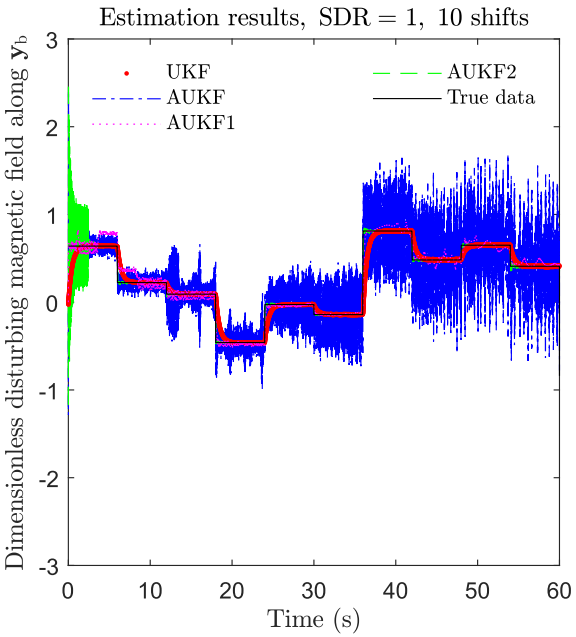

FIGURE 7. Disturbing magnetic field along y_b with 10 disturbing magnetic field shifts when the SDR is equal to one.

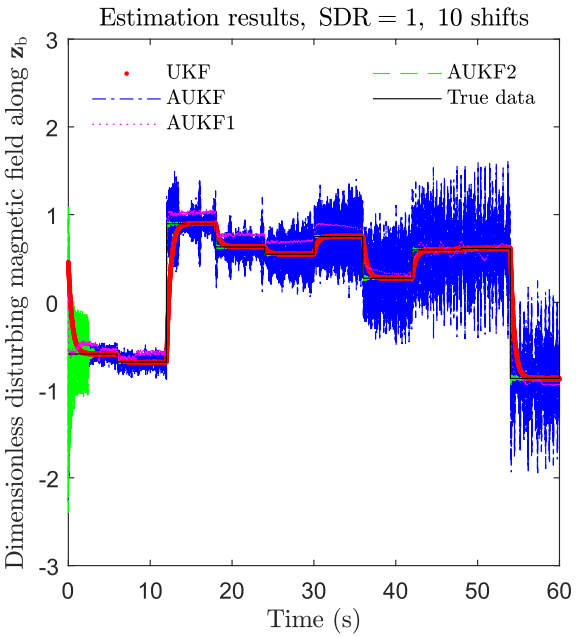

FIGURE 8. Disturbing magnetic field along z_b with 10 disturbing magnetic field shifts when the SDR is equal to one.

Figure 7 to Figure 10. Figure 7 and Figure 8 show the disturbing magnetic field along $\mathbf{y}_b$ and the disturbing magnetic field along $\mathbf{z}_b$, respectively. Ten shifts are applied in the simulation within the simulation time. Because the disturbing magnetic field along $\mathbf{y}_b$ and $\mathbf{z}_b$ are employed as state variables by (8), the shifts that are used to simulate interfering magnetic field mutations will produce a state exception and can be used to test the adaptability of the algorithms to state mutation. Figure 9 presents the estimated results of the rolling angular velocity. For the simulation in the paper, direct measurement

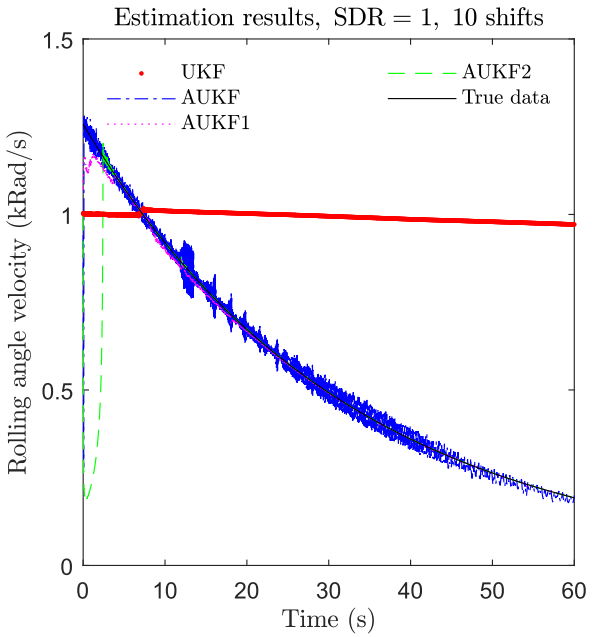

FIGURE 9. Rolling angle velocity with 10 disturbing magnetic field shifts when SDR is equal to one.

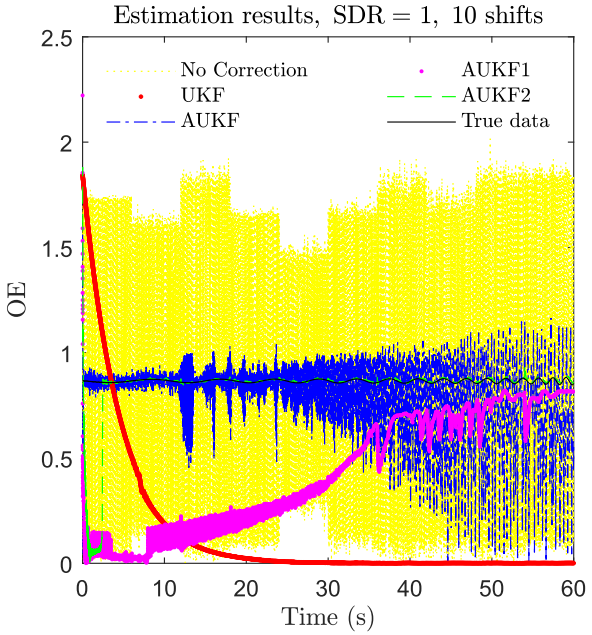

FIGURE 10. OE with 10 disturbing magnetic field shifts when SDR is equal to one.

data about the angular velocity of rolling are not available. However, the rolling angular velocity is a very important state variable for estimation. In the following simulation process, the failure of most algorithms is attributed to the inability to accurately predict the rotational velocity of roll. Figure 10 presents the OE estimated by UKF, AUKF, AUKF1 and AUKF2. For comparison purposes, the true value of the OE and the OE value obtained using uncorrected data are also presented.

As shown in Figure 7 to Figure 10, the conventional UKF, which is indicated by red dot, failed to estimate the rolling angular velocity. The UKF is the application of UT in the framework of KF and retains the disadvantage of KF. The weight of new data in prediction process is too small for UKF to effectively track the change of signal. This is the reason why the UKF failed in Figure 9. And OE is the vector sum of the geomagnetic projection along two lateral measuring axes. Since UKF cannot accurately estimate the roll angular velocity, it cannot correctly estimate the geomagnetic field projection along the relevant two lateral sensitive axes. Thus, the conventional UKF also failed in Figure 10. A feasible method to overcome this disadvantage is to increase the state covariance matrix by a fading factor so that the new data has a larger proportion in the estimation results. And the MCC [36] is one method of determining the fading factor. The AUKFs mentioned in Figure 7 to Figure 10 have different performance. The AUKF listed in Table 3 becomes unstable over time. The estimation results obtained by AUKF1, which are listed in Table 4, deviate from the true value in the initial stage of the simulation. The OE estimated by AUKF1 is not correct in the simulation interval. AUKF2 listed in Table 5 obtains reasonable estimated results, which show agreement with the true values. The yellow dotted line in Figure 10 indicated that the OE cannot be correctly obtained by using the noisy and interrupted measurement data. The OE is the projection of the geomagnetic field in plane $\mathbf{y}_b O \mathbf{z}_b$ and is the extreme value obtained using all ratio methods. This value is equal to the vector addition of the data from the lateral sensors and is equal to the ratio defined by (6). An accurate estimation of OE indicates that the influence of the disturbing magnetic field is totally eliminated, and the ratio utilized by all ratio methods can be accurately calculated. Based on the algorithm of trigonometric functions, the ratio defined in this paper can be converted to or from the ratio defined in other ratio methods. Thus, the ratio determined using the proposed method can be transformed and substituted into the methods used to perform attitude estimation. The simulation results presented in Figure 10 indicated that a proper filtering process after using an AD converter and before ratio methods is necessary for the sensitive geomagnetic data; the AUKF can be used to distinguish and eliminate the disturbing data in the data flow; and the algorithm that performs UT once in each loop is better than those transformed twice in this case.

As mentioned in subsection IV-B, the SDR is not a typical signal noise ratio (SNR). The SDR is a factor between the geomagnetic signal and the disturbing magnetic field. For the determined AD conversion circuits, the SDR will affect the SNR via amplification. Based on (26), the amplitude of the total signal is limited to $2^{n_{ad}-1} r_{fs}$. If the amplitude of the noise is approximately defined as $2^{n_{ad}-1} r_{fs} r_{sd} (1 + r_{sd})^{-1} r_{sn}^{-1}$, then the SNR can be presented as $r_{sn} (1 + r_{sd})^{-1} r_{sd}^{-1}$. For a determined r_{sn}, when the SDR is equal to 0.1 the SNR is approximately 11 times r_{sn}; when the SDR is equal to 10, the SNR is approximately 1.1 times r_{sn}.

In this subsection, the effect of SDR is compared by simulations with different r_{sd}. All algorithms mentioned in this article are compared. The OE calculated by the data

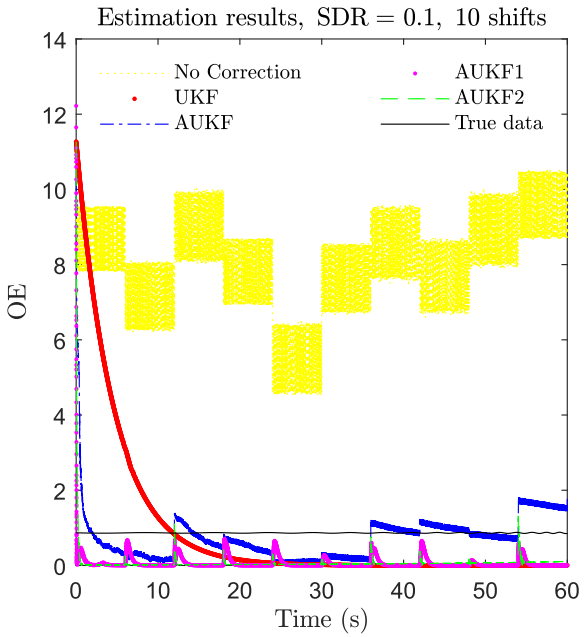

FIGURE 11. Estimation results with 10 disturbing magnetic field shifts when the SDR is equal to 0.1.

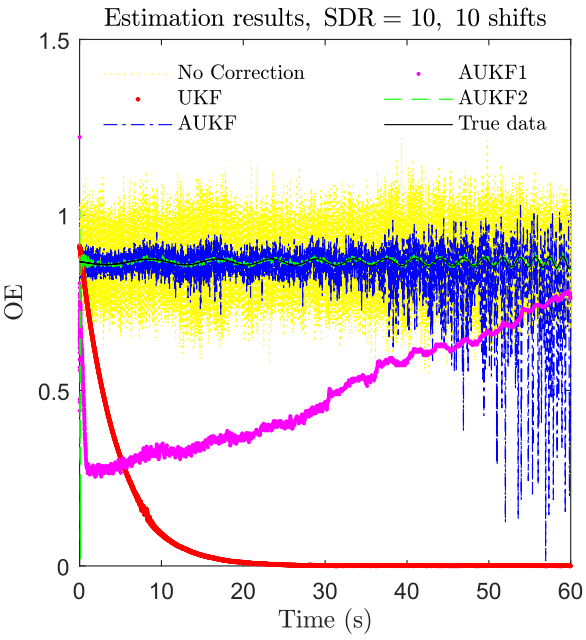

FIGURE 12. Estimation results with 10 disturbing magnetic field shifts when the SDR is 10.

before and after filtering is presented in Figure 11 and Figure 12.

As shown in Figure 11, when the SDR is 0.1, all filters failed. Although the filter denoted as AUKF2 obtained the correct estimate, the amount of time required in this case was excessive. The small SDR means large disturbing magnetic fields but a small random noise. The failure in this condition indicated that although the proposed filter has adaptability with regards to random noise and state outliers, large state anomalies can cause the filter to need a longer amount of time to obtain correct estimates, which limited the application for fast convergence. For the filter to work better, the disturbing magnetic fields need to be suppressed. This requirement is common among most geomagnetic measuring systems. For the satisfactory performance when the SDR is equal to one, as shown in Figure 10, the proposed filter is better than the other adaptive UKFs mentioned in the paper.

As shown in Figure 12, the proposed filter, which is denoted as AUKF2, achieved excellent estimation results when SDR is ten. Other filters do not achieve the desired purpose. The conventional UKF is too robust to follow rapid changes. The AUKF remain unstable. The filter used UT twice in one loop and denoted as AUKF1, requires a long time to converge. A large SDR means small state disturbances and large measurement noise. Note that the initial parameters of the filter always utilized the data listed in Table 6 and do not change with the SDR. The satisfactory performance of AUKF2 indicated that the proposed filter has excellent adaptability to unidentified noise.

V. CONCLUSION

The primary objective of this study was to eliminate the signal offset caused by disturbing the magnetic field that occurs after launch. For the ratio methods of attitude estimation that use magnetic sensors, the geometric interpretation of the extreme value was discussed by studying the projection of the local geomagnetic field on the intersecting surface of a body. The physical significance of the ratio, which is the key characteristic in all ratio methods, was clarified. A new ratio that can be transformed to or from the existing ratios was defined to ensure numerical stability and realize online correction. The variation in the outputs of the sensors was proved to be a harmonic motion by introducing the attitude equations of the motion of the object, with the assumption that the spindle is fixed or in slow motion. An approximate state model was presented to realize bias elimination and ratio estimation. The usage of the ratio defined in the paper was discussed. The state equations were reformulated to a step-by-step form for the KF. The state variable that pertains to the rolling angle velocity was substituted into the expression of one parameter and an exponent function to ensure convergence of the filter. Simulations were performed to verify the effect of the proposed filter. The true data that was employed as reference was generated by projecting the magnetic fields, including the geomagnetic and the disturbing magnetic fields, to the measurement frame constrained by a dynamics model of the spinning object. The signal amplification and AD conversion processes are also considered. In this paper, the factor SDR is defined as the ratio between the geomagnetic signal and the disturbing magnetic field. The influence of SDR on the state disturbance and measurement noise in a measured signal is discussed. Several algorithms of adaptive UKFs are discussed and their performances are compared by simulation results. The data before and after filtering are used to calculate the OE, which is the largest component of the geomagnetic field in the cross-section of

the projectile body. The comparison indicated the following findings: a proper filtering process after application of an AD converter and before utilization of ratio methods is necessary; the state function and the measurement function presented in the paper for a spin-stabilized projectile in geomagnetic signal filtering are correct; and the algorithm that updates sigma points once in each loop and only scales the prediction state covariance matrix is more efficient than a conventional UKF and other adaptive UKF algorithms mentioned in the paper. Although the proposed filter is developed for the ratio methods, it has the ability to provide clean data for other geomagnetic attitude measurement methods. Thus, it can be applied to an extensive range. A combination of geomagnetic and gyroscopic data may be useful. The gyroscopic can provide the measurement data of the rotation velocity for the proposed filter and accelerate the convergence of the filter, and the convergent filter can provide an estimation of the rolling angular velocity to eliminate the drifting of the gyroscopic or a long time deviation. These topics will be the focus of subsequent research.

AUTHOR CONTRIBUTIONS

Wei Wang contributed to providing the concept and design of the manuscript, performing the simulations, and drafting and revising the manuscript. Yulin Liu contributed to providing the introduction of the ng the manuscript.

Compliance with ethical standards Conflict of Interest The authors declare that they have no conflict of interest concerning the publication of this manuscript.

REFERENCES

[1] P. Hongfeng, P. Mengchun, W. Wei, Z. Qi, and L. Shitu, "Error calibration of three axis magnetometer based on Gauss-Newton iteration algorithm," *Chin. J. Sci. Instrum.*, vol. 34, no. 2, pp. 1506–1511, 2013.

[2] F. Liu, Z. Su, H. Zhao, Q. Li, and C. Li, "Attitude measurement for high-spinning projectile with a hollow MEMS IMU consisting of multiple accelerometers and gyros," *Sensors*, vol. 19, no. 8, p. 1799, Apr. 2019. [Online]. Available: https://www.mdpi.com/1424-8220/19/8/1799/pdf

[3] W. Wan, X. W. Chen, X. F. Peng, W. H. Bai, J. M. Xia, H. Liang, X. M. Zhang, P. Xiong, T. Yang, Y. C. Cao, C. Yin, L. M. Zhao, and Y. Hong, "Overview and outlook of GNSS remote sensing technology and applications," *J. Remote Sens.*, vol. 20, no. 5, pp. 858–874, 2016.

[4] X. Tang, N. Gao, J. Hao, G. Zhang, J. Lin, and D. Tan, "Application of high-speed photography to experiment of warhead," *J. Projectiles, Rockets, Missiles Guid.*, vol. 30, no. 3, pp. 105–110, Jan. 2010.

[5] C. Liu and K. B. Ariyur, "Construction of a sun sensor for geolocation and orientation," in *Proc. 25th Int. Tech. Meeting Satell.-Division Inst. Navigat.*, Nashville, TN, USA, Sep. 2012, pp. 3627–3635.

[6] K. Lima, I. M. Raimundo, Jr., A. M. S. Silva, and M. H. Pimentel, "Near and mid infrared optical sensors," *Quimica Nova*, vol. 32, no. 6, pp. 1635–1643, Jul. 2009. [Online]. Available: https://www.researchgate.net/publication/233972274

[7] C. Combettes, S. Changey, R. Adam, and E. Pecheur, "Attitude and velocity estimation of a projectile using low cost magnetometers and accelerometers," in *Proc. IEEE-ION Position Location Navigat. Symp.*, Monterey, CA, USA, Apr. 2018, pp. 650–657.

[8] D. Yuan, W. Yi, and J. Guan, "Roll attitude determination of spin projectile based on GPS and magnetoresistive sensor," *Math. Problems Eng.*, vol. 2017, no. 6, Jan. 2017, Art. no. 9638741. [Online]. Available: http://downloads.hindawi.com/journals/mpe/2017/9638741.pdf

[9] D. F. Long, J. Lin, X. M. Zhang, and J. Li, "Orientation estimation algorithm applied to high-spin projectiles," *Meas. Sci. Technol.*, vol. 25, no. 6, Jun. 2014, Art. no. 065001. [Online]. Available: https://iopscience.iop.org/article/10.1088/0957-0233/25/6/065001/pdf

[10] L. D. Fairfax and F. E. Fresconi, "Loosely-coupled GPS/INS state estimation in precision projectiles," in *Proc. IEEE/ION Position Location Navigat. Symp.*, Myrtle Beach, SC, USA, Apr. 2012, pp. 620–624.

[11] D. Li, and B. XiongZhu, "Roll angle measurement of spinning projectile based on non-orthogonal magnetic sensors," *Acta Armamentarii*, vol. 31, no. 10, pp. 1316–1321, 2010.

[12] R. de Celis and L. Cadarso, "Hybridized attitude determination techniques to improve ballistic projectile navigation, guidance and control," *Aerosp. Sci. Technol.*, vol. 77, no. 1, pp. 138–148, 2018.

[13] S. Bo, H. Xiaomao, W. Zhixing, C. Hejuan, and L. Baitan, "A study on a turns-counting sensor based on geomagnetism," *Acta Armamentarii*, vol. 24, no. 3, pp. 313–315, 2003.

[14] R. de Celis and L. Cadarso, "Attitude determination algorithms through accelerometers, GNSS sensors, and gravity vector estimator," *Int. J. Aerosp. Eng.*, vol. 2018, Feb. 2018, Art. no. 5394057.

[15] Y. Bao, G. Chen, and X. Cheng, "An economic full attitude detector for aerial vehicle with precomputed trajectory," *Measurement*, vol. 42, no. 2, pp. 208–213, Feb. 2009. [Online]. Available: http://www.sciencedirect.com/science/article/pii/S0263224108000985

[16] H. Goodarzi and M. Sabzehparvar, "Identifying pitching mode of aerial planting projectile by the use of image processing," *Proc. Inst. Mech. Eng. G, J. Aerosp. Eng.*, vol. 231, no. 14, pp. 2616–2633, Dec. 2017.

[17] Y. Zhou, X. Zhang, and W. Xiao, "Spinning projectile's angular measurement using crest and trough data of a geomagnetic sensor," *Meas. Sci. Technol.*, vol. 29, no. 9, Sep. 2018, Art. no. 095007. [Online]. Available: https://iopscience.iop.org/article/10.1088/1361-6501/aad0c7/pdf

[18] H. Zhao, Z. Su, F. Liu, C. Li, and Q. Li, "Magnetometer-based phase shifting ratio method for high spinning projectile's attitude measurement," *IEEE Access*, vol. 7, pp. 22509–22522, Feb. 2019.

[19] J. M. Maley, "Efficient attitude estimation for a Spin-stabilized projectile," *J. Guid., Control, Dyn.*, vol. 39, no. 2, pp. 339–350, 2016.

[20] S. Changey, D. Beauvois, and V. Fleck, "A Mixed Extended-Unscented Filter for attitude estimation with magnetometer sensor," in *Proc. Amer. Control Conf.*, Minneapolis, MN, USA, Jun. 2006, p. 6. [Online]. Available: https://ieeexplore.ieee.org/stamp/stamp.jsp?arnumber=1657158

[21] S. Changey, E. Pecheur, and T. Brunner, "Attitude estimation of a projectile using magnetometers and accelerometers," in *Proc. IEEE/ION Position, Location Navigat. Symp.*, Monterey, CA, USA, May 2014, pp. 1168–1173.

[22] X.-J. Yang, K.-I. Shi, and Y.-I. Wang, "Estimate of attitude and position of flying projectile controlled by combined guidance based on magnetometer/GPS," *Acta Armamentarii*, vol. 29, no. 2, pp. 169–173, 2008.

[23] R. V. Garcia, N. de Freitas Oliveira Matos, H. K. Kuga, and M. C. Zanardi, "Unscented Kalman filter for spacecraft attitude estimation using modified Rodrigues parameters and real data," *Comput. Appl. Math.*, vol. 35, no. 3, pp. 835–846, Oct. 2016.

[24] L. Baroni, "Kalman filter for attitude determination of a CubeSat using low-cost sensors," *Comput. Appl. Math.*, vol. 37, pp. 72–83, Dec. 2018.

[25] J. M. Maley, "Efficient attitude estimation for a spin-stabilized projectile," *J. Guid. Control Dyn.*, vol. 39, no. 2, pp. 339–350, Feb. 2016.

[26] G. Chang, "Robust Kalman filtering based on Mahalanobis distance as outlier judging criterion," *J. Geodesy*, vol. 88, pp. 391–401, Jan. 2014.

[27] G. Chang and M. Liu, "An adaptive fading Kalman filter based on Mahalanobis distance," *Proc. Inst. Mech. Eng. G-J. Aerosp. Eng.*, vol. 229, no. 6, pp. 1114–1124, May 2015.

[28] Y. Geng and J. Wang, "Adaptive estimation of multiple fading factors in Kalman filter for navigation applications," *GPS Solutions*, vol. 12, no. 4, pp. 273–279, Sep. 2008.

[29] J. Feng, Z. Wang, and M. Zeng, "Distributed weighted robust Kalman filter fusion for uncertain systems with autocorrelated and cross-correlated noises," *Inf. Fusion*, vol. 14, no. 1, pp. 78–86, 2013.

[30] B. Gao, G. Hu, S. Gao, Y. Zhong, and C. Gu, "Multi-sensor optimal data fusion based on the adaptive fading unscented Kalman filter," *Sensors*, vol. 18, no. 2, p. 488, Jan. 2018.

[31] Y. Meng, S. Gao, Y. Zhong, G. Hu, and A. Subicc, "Covariance matching based adaptive unscented Kalman filter for direct filtering in INS/GNSS integration," *Acta Astronautica*, vol. 120, pp. 171–181, Mar./Apr. 2016.

[32] F. Zha, S. Guo, and F. Li, "An improved nonlinear filter based on adaptive fading factor applied in alignment of SINS," *Optik*, vol. 184, pp. 165–176, May 2019.

[33] P. Baranov, V. Baranova, S. Uchaikin, and Y. Pisarenko, "Creating a uniform magnetic field using axial coils system for calibration of magnetometers," in *Proc. 10th IEEE Int. Sci. Tech. Conf. Dyn. Syst., Mech. Mach.*, Omsk, Russia, Nov. 2016, pp. 1–5.

[34] D. Long, X. Zhang, X. Wei, Z. Luo, and J. Cao, "A fast calibration and compensation method for magnetometers in strap-down spinning projectiles," *Sensors*, vol. 18, no. 12, p. 4157, Nov. 2018. [Online]. Available: https://www.mdpi.com/1424-8220/18/12/4157/pdf
[35] B. Grandvallet, A. Zemouche, M. Boutayeb, and S. Changey, "Real-time attitude-independent three-axis magnetometer calibration for spinning projectiles: A sliding window approach," *IEEE Trans. Control Syst. Technol.*, vol. 22, no. 1, pp. 255–264, Jan. 2014.
[36] Z. Deng, L. Yin, B. Huo, and Y. Xia, "Adaptive robust unscented Kalman filter via fading factor and maximum correntropy criterion," *Sensors*, vol. 18, no. 8, p. 2406, Jul. 2018. [Online]. Available: https://www.mdpi.com/1424-8220/18/8/2406/pdf
[37] Z. P. Han, *External Ballistics of Projectiles*. Beijing, China: Beijing Institute of Technology Press, 2008.
[38] S. J. Julier and J. K. Uhlmann, "Unscented filtering and nonlinear estimation," *Proc. IEEE*, vol. 92, no. 3, pp. 401–422, Mar. 2004.

WEI WANG received the B.S. degree in aircraft design and the Ph.D. degree in dynamics and control from the College of Aerospace Engineering, Nanjing University of Aeronautics and Astronautics, Nanjing, China, in 2001 and 2007, respectively. He is currently a Lecturer with the Nanjing University of Science and Technology. His research interests include dynamics, mechanics of flight, measuring, and instrumentation.

YULIN LIU received the B.S. degree in information countermeasure technology from the School of Electronic and Optical Engineering, Nanjing University of Science and Technology, Nanjing, China, in 2018, where he is currently pursuing the M.S. degree with the National Key Laboratory of Transient Physics. His research interests include projectile attitude determination and FPGA equipment research.